THE JOURNAL OF PHYSICAL CHEMISTRY C
A JOURNAL OF THE AMERICAN CHEMICAL SOCIETY

pubs.acs.org/JPCC

Article

First-Principles Study of Oxygen-Induced Disintegration and Ripening of Late Transition Metal Nanoparticles on Rutile-TiO_2(110)

Shiyan Cao, Xuting Chai, Sulei Hu,* and Wei-Xue Li*

Cite This: *J. Phys. Chem. C* 2022, 126, 8056−8064

Read Online

ACCESS | Metrics & More | Article Recommendations | Supporting Information

ABSTRACT: Under an industry-related high-temperature oxidation atmosphere, the structure and chemical states of metal nanocatalysts meeting sustainable development challenges change dramatically, deteriorating the activity and/or lowering the yield. Theoretically revealing the mechanisms of oxygen-induced structure evolution and establishing a framework to distinguish them are vital to improving the operando stability and rational design of metal nanocatalysts. Here, we studied the oxygen-induced disintegration and Ostwald ripening of Ni, Cu, Pt, Pd, and Ag nanoparticles on TiO_2(110) using first-principles-based thermodynamic and kinetic simulations. It was found that oxygen promotes Ostwald ripening via the formation of Ag/Ag−O and Pd intermediates on the support and volatile gaseous PtO_2 complexes, induces disintegration of Ni nanoparticles to Ni−O complexes, and leads to the formation of copper oxide. These differences in the deactivation pathways can be attributed to the dependence of the ripening activation energies and disintegration free energies on the interaction between metal atoms/complexes and TiO_2(110). Revealed knowledge and corresponding models provide valuable insights into the general mechanisms governing the structural evolution of supported nanocatalysts under reaction conditions.

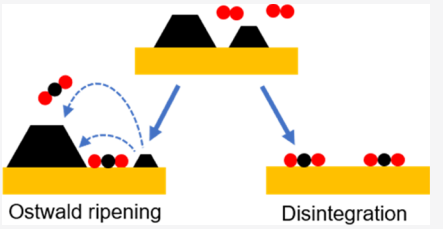

Downloaded via UNIV SCIENCE AND TECHNOLOGY CHINA on May 13, 2022 at 00:05:59 (UTC).
See https://pubs.acs.org/sharingguidelines for options on how to legitimately share published articles.

1. INTRODUCTION

The structural stability of heterogeneous nanocatalysts under reaction conditions is a common and essential issue in chemical conversions and environmental sustainment.[1−4] Metal nanocatalysts suffer from various dynamic changes under actual reaction atmospheres, such as segregation of components,[5,6] growth in size,[7−9] dispersion,[10−13] reversible and irreversible reshaping,[14−16] and phase change.[17,18] Usually, these structure evolutions are not isolated and greatly hinder the long-term applications of nanocatalysts with decreasing reactivity.[19] The rational design of nanocatalysts requires a deep understanding of the dynamical response mechanisms of nanoparticles (NPs) to reaction conditions.

Typically, metal nanocatalysts may form new phases under reaction conditions, including oxide under oxidation,[20,21] hydride under hydrogenation,[22] and carbide under a Fischer−Tropsch condition.[17] These transformations may boost the reactivity due to the formed metastable superstructure[21] or deactivate the catalysts due to the loss of the active metal phase.[23] Metal−reactant−support interplay may also lead to the disintegration of metal nanocatalysts into small clusters[15] or even single atoms,[24,25] which are generally used to regenerate the deactivated catalysts or synthesize the single-atom catalysts. Sometimes, reactant-induced disintegration may be inversed to the growth of nanocatalysts in size, leading to the deactivation of nanocatalysts due to the loss of active surface sites, via the detachment from and attachment onto NPs and diffusion transportation of metal atoms through the gas phase or on the support called as Ostwald ripening (OR).[26−28] These remarkable structural evolutions are essential features of nanocatalysis science, and they are also the price of high tunability and performance. However, insights into the competition essence and their dependence on the metal composition of these dynamic evolutions are still lacking.

Here, using Ni, Cu, Pt, Pd, and Ag as typical examples, we studied O_2-induced disintegration and OR through gaseous and surface intermediates of metal NPs on TiO_2(110) using thermodynamics and ripening kinetic simulations based on density functional theory (DFT) calculations. Specifically, we calculated the free energies of disintegration and the activation energies of the ripening intermediates and the corresponding half-life time (the time halving the initial particle number) of ripening as the criteria for these processes. The results show that the metal−oxygen complexes of Ni have a strong binding with support and the NPs can be dispersed under O_2; for Pd and Ag, the binding between their species and support is moderate and OR occurs through the surface intermediates; for Pt, the preferred PtO_2 species has a weak interaction with support and gaseous OR through gaseous intermediates is more preferred; for Cu, the formation of the oxide phase is relatively preferential to the disintegration process. These insights and corresponding theoretical models help the

Received: January 25, 2022
Revised: April 22, 2022
Published: May 4, 2022

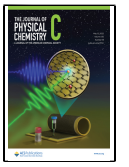

© 2022 American Chemical Society

https://doi.org/10.1021/acs.jpcc.2c00612
J. Phys. Chem. C 2022, 126, 8056−8064

identification of the dominant deactivation mechanisms of supported NPs under reaction conditions, potentially aiding the rational design of nanocatalysts.

2. METHODS

2.1. Oxygen-Induced Ripening Kinetics. For surface ripening of the supported NPs at a given radius R of the curvature, the rate equation under mean-field and steady-state approximation can be found in previous work.[29,30] We extended the rate equation to consider the influence of the reaction conditions, where the ripening intermediates might be changed from the metal atoms to the metal−reactant complexes on supports.[31] In the present work, we further investigated Ostwald ripening through the gas phases by the metal atom or the metal−reactant complexes. For completeness and simplification, all of these equations are unified and written as

$$\frac{dR}{dt} = A(R, T)\exp\left(-\frac{E_{act}}{kT}\right)\left[\exp\left(\frac{\Delta\mu(R^*)}{kT}\right) - \exp\left(\frac{\Delta\mu(R)}{kT}\right)\right] \quad (1)$$

where $A(R,T)$ is a pre-exponential factor that depends on contact angle θ of metal NPs, temperature T, and radius R of the curvature of the supported particles; E_{act} is the ripening activation energy; $\Delta\mu(R)$ is the chemical potential of atoms in metal NPs; and k is the Boltzmann constant.

For surface ripening, the corresponding pre-exponential factor is defined as

$$A(R, T) = \frac{XY}{X + Y}\frac{\nu_s\Omega}{4\pi a_0^2\alpha_1 R}\frac{1}{} \quad (2)$$

where $X = 2\pi a_0 R\sin(\theta)$, $Y = 2\pi a_0^2/\ln[L/R\sin(\theta)]$, a_0 is the lattice constant of the support surface, L is the diffusion length of the intermediates, ν_s is the vibrational frequency of the intermediates, $\alpha_1 = (2 - 3\cos\theta + \cos^3\theta)/4$, and Ω is the molar volume of the bulk metal atom.

For gaseous ripening, the corresponding pre-exponential factor is defined as

$$A(R, T) = \frac{\alpha_2\chi\Omega p_0}{\alpha_1\sqrt{2\pi mkT}}\left(\frac{p_{O_2}}{p_0}\right)^{n/2} \quad (3)$$

where $\alpha_2 = (1 - \cos\theta)/2$, m is the mass weight of corresponding ripening intermediates, p_0 and p_{O_2} are the standard pressure and the partial pressure of O_2, and n is the oxygen atom number in the intermediate MO_n. χ is the sticky coefficient, which represents the fraction of gaseous intermediates formed or the reverse dissociative process and varies from 0.7 to 1 for oxygen coverage on metal surfaces less than 3/9 ML.[32] For typical conditions where the gas-phase ripening might happen, T varies from 500 to 900 K and oxygen partial pressure p_{O_2} from 10^{-4} and 10^{-1} bar, and oxygen coverage on Pt(111) surfaces is less than 3/8 ML (Figure S1). In the present work, we chose a constant of 0.75 for the sticky coefficient unless stated otherwise. The ripening intermediates of the above mechanisms are single-metal atoms. For the intermediate with multiple metal atoms, such as Ag_2O, both prefactor and activation energy that describe the properties of intermediates will change accordingly.

For NPs at a given R, $\Delta\mu(R)$ of atoms in NPs with respect to the bulk metal is described by the Gibbs−Thomson equation

$$\Delta\mu(R) = \frac{2\gamma\Omega}{R} \quad (4)$$

where γ is the surface energies of bulk metals. In this work, the average surface energies come from the DFT calculation database.[33] The effect of reactant adsorption on γ and $\Delta\mu$ is evaluated and shown in the Supporting Information.

The term in the bracket, the exponential difference of $\Delta\mu(R)$, describes the growth direction and tendency among the particles with different sizes. A critical radius R^* is defined as a radius where particles neither grow nor shrink. This critical radius represents an "average" of particles. Any particles larger than the critical radius will grow and those smaller will shrink.

The ripening kinetics was simulated for a given initial particle ensemble with 1500 particles. The initial particle size distribution of the NPs follows a Gauss distribution with an average diameter and standard deviation of 4 and 0.6 nm, respectively. The influence of the particle morphology is neglected in this work and the contact angles of all particles are set to 90°.

2.2. DFT Calculations. To evaluate the free energies and effective activation energies of Ni, Cu, Pt, Pd, and Ag on TiO_2, DFT calculation was performed by the Vienna Ab initio Simulation Package (VASP 5.4).[34−36] The projector-augmented wave method[37] and Perdew−Burke−Ernzerhof (PBE) functional[38] were used. The van der Waals effect or dispersion correction is evaluated using opt−PBE−vdw functionals for Ni, Pt, and Ag and their metal−oxygen complexes in Table S1, and does not affect the trend of the systems involved. The cutoff energy of the plane wave basis set was set to 400 eV. Spin polarization is explicitly performed for both surface structures and gaseous molecules. Optimized rutile parameters are a = 4.598 Å and c = 2.958 Å, which is in good agreement with experimental values a = 4.593 Å and c = 2.959 Å.[39] In this work, we use experimental cohesive energies[40] for the supported metal atoms and complexes. The oxygen vacancies are not considered in this work because the oxidative atmosphere is considered here.

Adsorption structures of the ripening intermediates on rutile TiO_2(110) were described by a (2 × 4) slab of four Ti−O layers with a 15 Å vacuum layer in the case where dipole correction is considered. The top two layers are relaxed for optimization and the bottom two layers are fixed. Monkhorst−Pack k-points were set to 3 × 3 × 1. Systems were relaxed until the force on each atom was less than 0.02 eV/Å. The effect of Hubbard U correction was evaluated and is shown in Figure S2. At $U_{eff} = U - J$ = 3 eV, the formation energy of Pt decreases by 0.29 eV on the rutile (110). It is small compared to the difference of intermediates (2.71 eV for PtO_2 and Pt). Hence, the Hubbard U correction is not considered in this work. Isolated gaseous molecules (O_2, M, MO, MO_2) are optimized in a 15.0 Å × 15.1 Å × 15.2 Å cell to find the most stable structures.

To calculate the diffusion barriers of the ripening intermediates on the oxide surfaces, the climbing image nudged elastic band (CI-NEB)[41] and dimer[42] methods were used to find transition states (TSs). For CI-NEB, at least seven images, including the initial and final states, were used and all of the TSs were validated by showing a single imaginary mode in the vibrational analysis.

https://doi.org/10.1021/acs.jpcc.2c00612
J. Phys. Chem. C 2022, 126, 8056−8064

3. RESULTS AND DISCUSSION

3.1. Disintegration. Under oxygen conditions, the supported metal nanocatalysts may be decomposed into metal−oxygen complexes, which detach from the nanocatalysts and anchor at the support surface as thermodynamically stable products. From a theoretical point of view, we can evaluate the difficulty of decomposition of supported nanocatalysts by calculating their disintegration Gibbs free energy ΔG_{NP}^{dis} [31] into the complex MO_n as

$$\Delta G_{NP}^{dis}(R, T, p) = E_f^s - 0.5n \times \Delta\mu_{O_2}(T, p) - \Delta E_{NP}(R) - TS \quad (5)$$

The formation energy E_f^s of the surface complex MO_n was calculated via

$$E_f^s = E_{slab}(MO_n) - E_{slab}(\text{oxide}) - E_B(M) - 0.5n \times E(O_2) \quad (6)$$

where $E_{slab}(MO_n)$, $E_{slab}(\text{oxide})$, $E_B(M)$, and $E(O_2)$ are the DFT-calculated total energies of the surface adsorbed monomers MO_n with the oxide surface, the slab of the oxide surface, the bulk metal atom, and gaseous O_2, respectively. $\Delta\mu_{O_2}(T,p)$ is the chemical potential of O_2 under given temperature T and oxygen pressure p, which is obtained from the ASE library.[43] $\Delta E_{NP}(R) = \frac{3\gamma\Omega}{R}$ is the average energy per atom of a finite-sized NPs with respect to the bulk metal atom, where γ, Ω, and R are the surface energy of the NPs, molar volume of bulk metal atoms,[31] and the radius of the NPs, and S is the configurational entropy of the complexes on the support surface. As a typical example, for a coverage of 0.01, the estimated entropy contribution is $4.83 \times 10^{-4}T$ (unit is eV).[44]

For the disintegration, the energetics of the corresponding metal atom and its complex with the reactant on the surface of the support is crucial. We calculated the most stable adsorption structures of these surface monomers, as shown in Figure 1 and the corresponding E_f^s of single atoms of Ni, Cu, Pt, Pd, and Ag and their complexes with one (MO) or two oxygen atoms (MO_2) on TiO_2(110) support based on eq 6, as listed in Table 1. The formation energies E_f^s(M) of these metal atoms

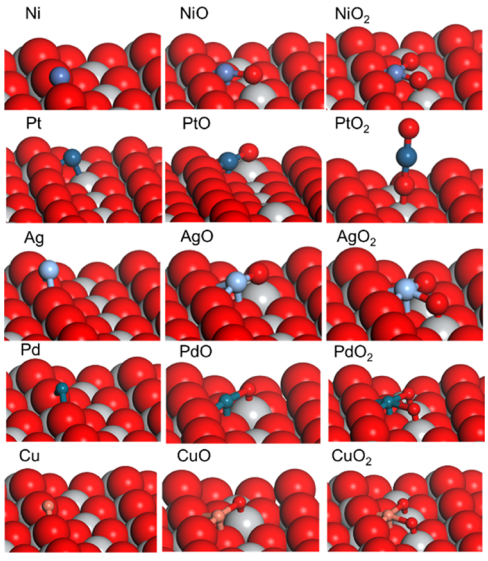

Figure 1. Most stable adsorption structures of surface monomers on rutile TiO_2(110).

Table 1. Formation Energies of Various Adsorbed Metal Monomers (E_f^s) on the TiO_2(110) Surface[a]

metal	E_f^s(M), eV	E_f^s(MO), eV	E_f^s(MO_2), eV	ΔH_f^o(ox), eV
Ni	1.57	−0.58	−0.38	−2.51[45]
Cu	1.76	0.14	1.12	−0.89[46]
Pt	3.92	2.06	1.21	−1.39[47]
Pd	2.41	1.09	1.22	−1.22[48]
Ag	2.17	1.47	2.95	−0.16[49]

[a]Corresponding formation energies (ΔH_f^o(ox)) of the bulk oxides NiO, $CuO_{1/2}$, PtO_2, PdO, and $AgO_{1/2}$ are obtained from experiments at 298.15 K.

corresponding to the bulk metals are 1.57, 1.76, 3.92, 2.41, and 2.17 eV, respectively. These values are larger than 1.5 eV, indicating that the formation of these supported metal atoms is not thermodynamically feasible on TiO_2(110) with respect to the bulk metals. With the introduction of O_2, supported metal atoms can coordinate with oxygen, forming metal−oxygen complexes, such as MO (Ni, Pd, Cu, Ag) and MO_2 (Pt). The corresponding $E_f^s(MO_n)$ is significantly reduced, especially, negative E_f^s(NiO) of −0.58 eV versus E_f^s(Ni) of 1.57 eV and near-zero E_f^s(CuO) of 0.14 eV versus E_f^s(Cu) of 1.76 eV. This reduction in the formation energy indicates the stabilizing effect of supported metal atoms by the additional coordination with oxygen, which suggests the feasibility of their formation with respect to their bulk metals under oxygen conditions. We noted that supported complexes with multiple metal atoms may also form, as discussed in the Supporting Information.

To further confirm the disintegration of metal NPs induced by the oxygen atmosphere, we calculated ΔG_{NP}^{dis} of these five metals and plotted their dependence on the T, p, and particle size based on eq 5. Figure 2a shows ΔG_{NP}^{dis} of Ni NPs into NiO complexes versus T under different ps of O_2 and particle diameters. For a Ni NP with a diameter of 4 nm at p of O_2 of 10^{-7} bar, ΔG_{NP}^{dis} increases from −0.37 to 0.78 eV as T increases from 400 to 1200 K (blue line in Figure 2a). A zero-crossing point of 670 K represents the upper limit of disintegration temperature of Ni NP, considering that the formed complex is not stable at higher T. For the same diameter of 4 nm, as p of O_2 increases to 10^{-1} bar (black line in Figure 2a), this upper limit increases to 1140 K, indicating that the heat resistance of the formed complex becomes stronger at a higher p. As the diameter increases from 4 to 8 nm at the same p of 10^{-1} bar, the upper limit of disintegration temperature decreases slightly to 1020 K (red line in Figure 2a), indicating that the disintegration becomes harder for a larger NP.

To check the difference of metals, we plotted their ΔG_{NP}^{dis} versus T at a diameter of 4 nm and p of 0.1 bar in Figure 2b. Compared to Ni, which shows thermodynamic feasibility of forming a stable complex of NiO, ΔG_{NP}^{dis} of Pt, Pd, and Ag is positive and larger than 1.50 eV, indicating that disintegration will not occur from 400 to 1200 K. For Cu, the ΔG_{NP}^{dis} at 400 K and 0.1 bar is only 0.17 eV. This value is slightly positive, therefore under a condition with a higher p, lower T, and smaller size, the disintegration of Cu NPs may become thermodynamically favored, which is consistent with the experimental observation that Cu clusters disappeared at 500 K on exposure to oxygen.[50] The trend of these metals of Ni < Cu < Pd < Ag < Pt on the disintegration is mainly correlated to

https://doi.org/10.1021/acs.jpcc.2c00612
J. Phys. Chem. C 2022, 126, 8056−8064

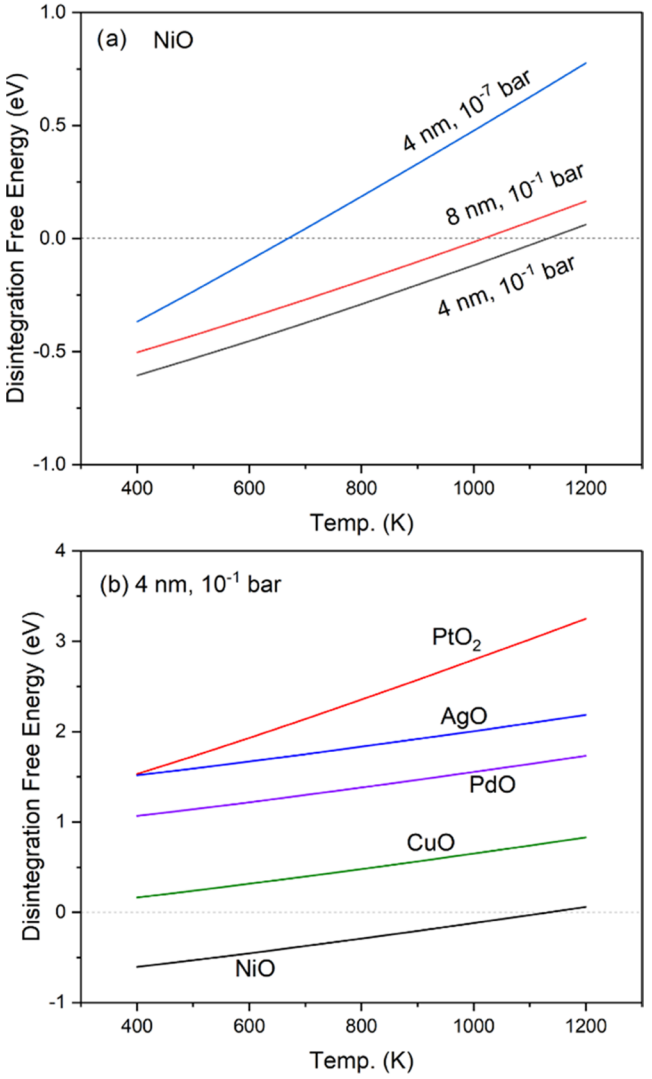

Figure 2. Disintegration free energies of nanoparticles versus temperature under different *ps* of O_2 and particle diameters for Ni (a) and for Ni, Cu, Pt, Pd, and Ag under 0.1 bar O_2 and a particle diameter of 4 nm (b).

the binding energy between the metal−oxygen complex and support, considering the same order of −3.04 eV (NiO) < −2.91 eV (CuO) < −2.54 eV (PdO) < −2.14 eV (AgO) < −0.34 eV (PtO_2), as shown in Figure 3.

We noted that under an oxygen atmosphere, O_2 may dissociate and further diffuse into the metal surface, which forms oxide layers. To access the oxidation tendency of these metals, the standard enthalpies of formation ΔH_f^o of their oxide[45−49] are listed in Table 1. The oxides of Ni, Cu, Pd, and Pt have negative ΔH_f^o, and oxides of these metals can be formed under oxygen conditions, while the oxide of Ag can be easily reversed back to metals when the temperature changes since its ΔH_f^o is just −0.16 eV. To thermodynamically assess the potential competition of disintegration and oxidation, we plotted the Gibbs free energy of oxidation ΔG^{ox} and ΔG^{dis} of these five metals versus *T* with respect to the bulk metals, as shown in Figure S3. We found that as *T* increases from 400 to 1200 K, these five metals show a lower oxidation free energy than disintegration, indicating that oxidation of metals is always thermodynamically more favorable than disintegration into supported metal complexes if the kinetics is allowable.

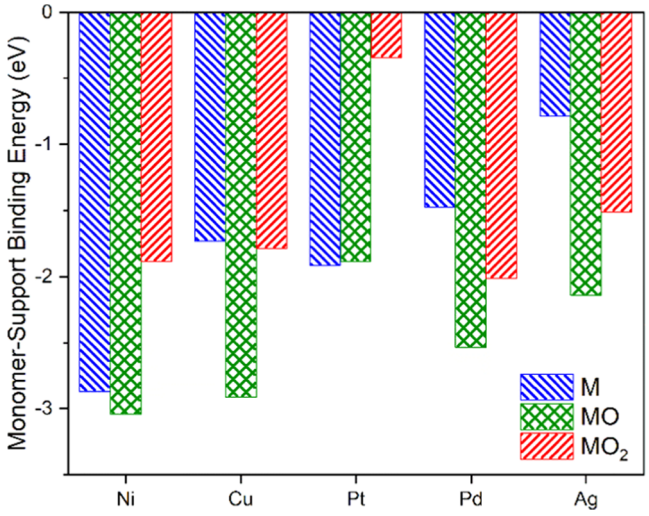

Figure 3. Binding energies of the metal atom M (blue), the oxide molecules MO (green), and MO_2 (red) to TiO_2(110) at their most stable sites. All units are given in eV.

Specifically, for Ni, both ΔG_{ox} and ΔG_{NP}^{dis} are negative when *T* is below 1000 K, showing that both oxidation and disintegration are viable for Ni. Experimentally, for Ni NPs, simultaneous size shrinkage and formation of oxide were observed at room temperature and 1.3×10^{-10} bar O_2.[50] For Cu, ΔG_{ox} forming the oxidation phase Cu_2O is negative (exothermic), showing the feasibility of oxidation within 400−1200 K. The STM observations found that the Cu clusters undergo the oxidation and flattening of the morphology into a 2D structure under an oxygen atmosphere.[51] This process is also corroborated by XPS experiments.[52] For Pt, Pd, and Ag, ΔG_{NP}^{dis} is always positive and ΔG_{ox} becomes negative at *T* smaller than 770, 1140, and 460 K, respectively, indicating that metal−oxygen complexes cannot exist thermodynamically as products of disintegration and the feasibility of oxidation under a relatively low *T*. Under the given *T* range of 400−1200 K, positive ΔG_{NP}^{dis} of Pt, Pd, and Ag is potentially accompanied by the possibility of particle growth in size due to the diffusion transportation of these unstable complexes through the gas phase or the support surface.

3.2. Surface and Gaseous Ripening. When the monomers (metal atoms or metal−reactant complexes) are thermodynamically unstable ($\Delta G_{NP}^{dis} > 0$, as discussed in the previous section), they may diffuse as surface intermediates on the support (surface route) or desorb via the volatile complex in the gas phase (gaseous route) and recombine to metal particles. This fact leads to the growth of larger particles at the cost of smaller particles, namely, Ostwald ripening (OR). In previous works,[31] we developed the ripening kinetic methods, which are based on the mean-field approximation and steady-state assumption and the data obtained by first-principles calculations. The influences of particle size distribution,[53] reactant,[54] support phase, and morphology[55] were evaluated. To explore the competition of different ripening routes, we performed the thermodynamic analysis and the ripening kinetics simulations, and the corresponding methodology details are shown in Section 2. Under the steady-state approximation, the detachment and reattachment of the metal atoms reach a steady state, which allows us to use the activation free energy ΔG_{act} of the ripening intermediates to characterize the OR process.

https://doi.org/10.1021/acs.jpcc.2c00612
J. Phys. Chem. C 2022, 126, 8056−8064

For the surface ripening route, the corresponding activation free energy ΔG^{s}_{act} is the sum of the formation energy E^{s}_{f} and the diffusion barrier E^{s}_{d} of the ripening intermediates MO_n on oxide surfaces, at the cost of O_2 free energy in the gas phase. This activation energy represents the upper limit of the barrier required for the metal atoms to break off from the particles. Ripening intermediates might be the metal monomer ($n = 0$) or the metal−oxygen complexes, and the corresponding activation (free) energy is calculated by

$$\Delta G^{s}_{act} = E^{s}_{f} + E^{s}_{d} - 0.5n \times \Delta\mu_{O_2}(T, p) \quad (7)$$

where E^{s}_{f} is the formation energy of surface intermediates, as defined in eq 6. For the gas-phase ripening, the activation free energy of a gaseous intermediate ΔG^{s}_{act} is defined by

$$\Delta G^{g}_{act} = E^{g}_{f} - 0.5n \times \Delta\mu_{O_2}(T, p_0) - \Delta\mu_{M}(T) + \Delta\mu_{MO_n}(T, p_0) \quad (8)$$

where E^{g}_{f} is the formation energy of gaseous intermediate $E^{g}_{f} = E_{Mo_n} - E_{M} - 0.5n \times E_{O_2}$, where E_{MO_n} and E_{M} are the DFT-calculated total energies of the gaseous MO_n and M. $\Delta\mu_{M}$ and $\Delta\mu_{MO_n}$ are the chemical potential of bulk metals and gaseous MO_n molecules, which are obtained from the thermodynamic data[56,57] and ASE library, respectively.[43]

To obtain the ripening activation energies based on eqs 7 and 8, we calculated E^{g}_{f} for gaseous intermediates and E^{s}_{f} (Table 1) and E^{s}_{d} for surface intermediates (Pt, PtO, PtO_2, Ag, AgO, Pd, PdO) and plotted them in Figure 4. Structures of the diffusion transition state are shown in Figure S4. Generally, isolated metal atoms are unstable in the gas phase due to their relatively high E^{g}_{f}, for example, 5.84 eV for Pt. With the introduction of O_2 or support, the metal atom as an intermediate is stabilized via a gaseous complex or a supported metal adatom/complex with a lower formation energy (drops to 1.55 eV for gaseous PtO_2, or 1.21 eV for supported PtO_2). E^{s}_{d} of single-metal atoms and linear PtO_2 is less than 0.3 eV during diffusion (Table S4), but E^{s}_{d} of PtO (0.79 eV) is higher because more bindings are involved during the diffusion. For Pd, the supported PdO has the lowest formation energies (1.19 eV) in surface intermediates and gaseous PdO_2 has the lowest E^{g}_{f} (3.24 eV). For Ag, the supported AgO or gaseous Ag atoms have the lowest E_f (1.47 and 2.95 eV) for both surface and gaseous intermediates. We also calculated E^{s}_{f} of AgO_2 and found this value was 1.48 eV higher than that of AgO, indicating that AgO_2 is negligible as a ripening intermediate. Hence, we did neither further calculate the diffusion barrier of AgO_2 nor simulate the corresponding ripening kinetics. We noted that supported complexes with multiple metal atoms may also exist. Their formation can be thermodynamically more favored but their diffusion barrier becomes higher, as discussed in the Supporting Information.

With these formation energies and diffusion barriers, we calculated the corresponding ΔG_{act} for both surface and gaseous OR. Figure 5a shows how ΔG^{s}_{act} changes with T for Pt and Ag in 0.1 bar O_2 via a surface OR mechanism. Compared to the surface intermediates of Pt and PtO, PtO_2 (blue solid line) has the lowest ΔG^{s}_{act} from 500 to 900 K and 0.1 bar (2.97 eV at 700 K and 0.1 bar) and is the most favored intermediate. However, for Ag, the ΔG^{s}_{act} of Ag atoms (black dash line) is

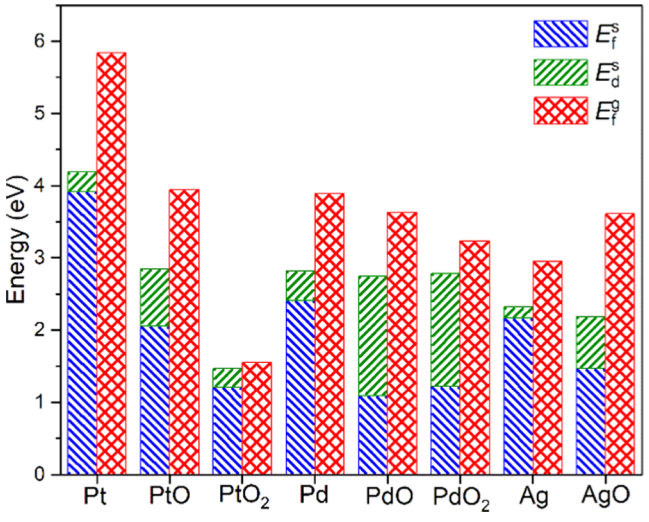

Figure 4. Formation energies of the metal atoms and oxide molecules on support E^{s}_{f} (blue) and in gas-phase support E^{g}_{f} (red). The diffusion barriers E^{s}_{d} (green) of the metal atoms and oxide molecules on support. All units are given in eV.

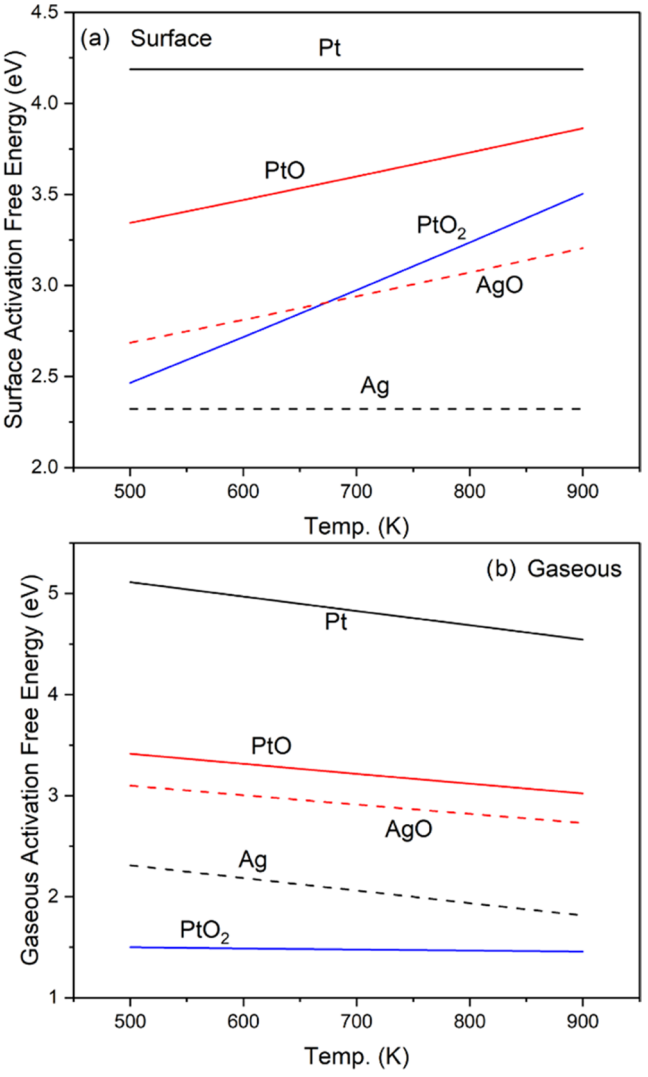

Figure 5. Activation free energies of surface (ΔG^{s}_{act}, a) and gaseous (ΔG^{g}_{act}, b) ripening intermediates of Pt and Ag using eq 8. The O_2 pressure is 0.1 bar.

https://doi.org/10.1021/acs.jpcc.2c00612
J. Phys. Chem. C 2022, 126, 8056−8064

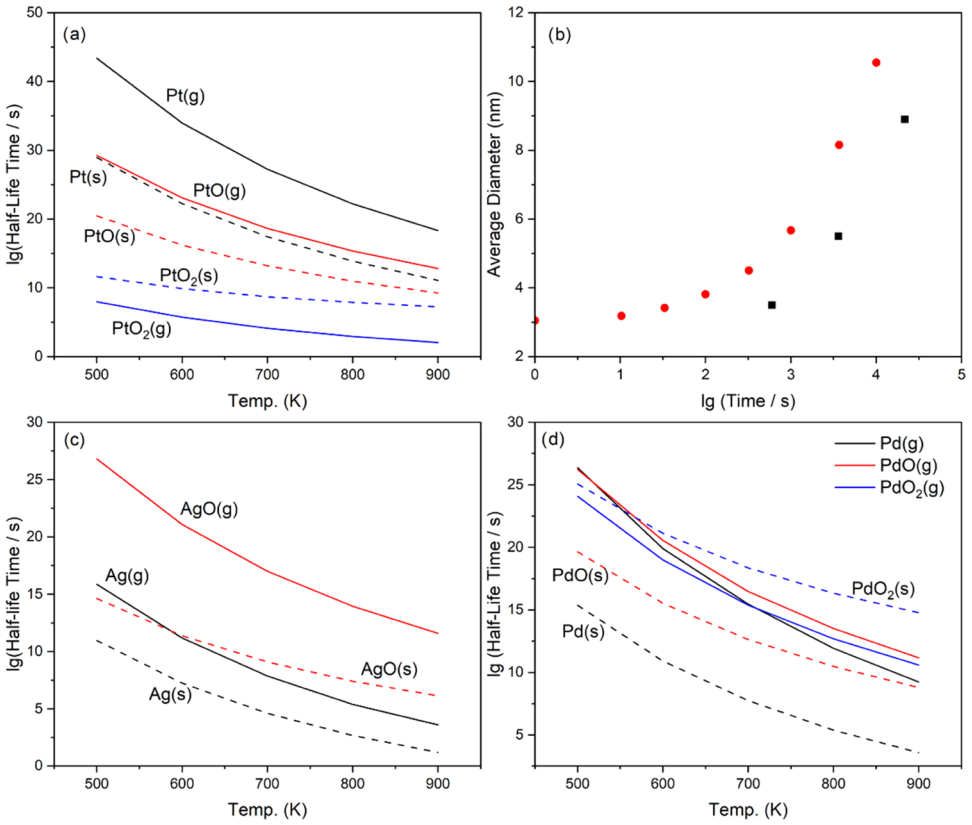

Figure 6. Simulated ripening half-life time of Pt (a), Ag (c), and Pd (d) NPs under O_2 pressure (0.1 bar), the initial average particle diameter (4 nm), and the corresponding standard deviation (0.6 nm). (b) Time dependence of average diameters of Pt NPs simulated under an oxygen condition based on gaseous (red circles) OR and obtained from the experiment[58] (black squares, the support is SiO_2) with the same condition of initial average size (3 nm), standard deviation (0.8 nm), temperature (873 K), and oxygen pressure (0.04 bar).

lower than that of a AgO complex (red dash line) under 500−900 K and 0.1 bar O_2. This result indicates that a Ag atom is favored instead of a AgO complex (as discussed above, AgO_2 and Ag_2O are not favored and are not considered again).

Similarly, the dependence of ΔG^{g}_{act} of Pt and Ag on T in a gaseous OR mechanism is shown in Figure 5b. It is found that ΔG^{g}_{act} of PtO_2 (blue solid line) is far lower than PtO and Pt as gaseous ripening intermediates and Ag (black dash line) is also lower than AgO as an intermediate. This result indicates that for Pt and Ag, the dominant ripening intermediates seem to be independent on whether the ripening mechanism is via surface or gaseous. In Figure S5, we calculated and plotted the dependence of ΔG^{s}_{act} and ΔG^{g}_{act} on T based on Pd, PdO, and PdO_2 as intermediates. However, the results show a mechanism-dependent intermediate: Pd for the surface mechanism and PdO for the gaseous mechanism. These results fully indicate the complexity of ripening mechanisms. It should be noted that as T increases, the ΔG^{s}_{act} of surface OR increases (Figure 5a), while that of gaseous OR decreases (Figure 5b). This difference mainly stems from whether the number of gaseous molecules is net consumed throughout the ripening kinetics. This fact indicates that as T increases, surface OR becomes less favored and gaseous OR may dominate, suggesting the potential crossover and switching of these two mechanisms.

To kinetically determine the competition between the surface and gaseous ripening mechanism of metal NPs, we simulated the ripening process based on different mechanisms and intermediates at different T of 500−900 K under 0.1 bar O_2. We further calculated the corresponding half-life time $t_{1/2}$ of ripening, the time needed for halving the number of particles, of Pt and plotted them in Figure 6a. The results indicate that the dominant intermediate for the gaseous mechanism is PtO_2 (blue solid line), considering that it has the smallest $t_{1/2}$ than PtO (red solid line) and Pt (black solid line) and that for gaseous is also PtO_2 (blue dashed line) based on the similar consideration under a T range of 500−900 K. For the competition of the surface and ripening mechanism, it is the gaseous OR mechanism that dominates the ripening route because $t_{1/2}$ of PtO_2 (g) is about 4 orders of magnitude lower than that of PtO_2 (s). This result shows that the introduction of O_2 greatly accelerates the ripening of Pt NPs accompanied by the change of intermediates from metal atoms (black dash line) to gas-phase PtO_2 complexes (blue solid line) when O_2 is involved. The simulated average diameter of Pt NPs based on the gaseous OR model using the same initial conditions basically reproduces the experimentally measured size dependence on time,[58] although with an average error of 0.4 orders of magnitude in time scale, as shown in Figure 6b. The vapor-phase ripening of Pt induced by O_2 is mainly driven by the strong interaction between the metal and the oxygen molecules, and the support plays a little role in the overall sintering behavior.

We also calculated $t_{1/2}$ of ripening for Ag and Pd and plotted them in Figure 6c,d. For Ag, considering that the surface OR mechanism based on a supported Ag atom as a ripening intermediate has the lowest $t_{1/2}$ than AgO as an intermediate under a T range of 500−900 K (Figure 6c), Ag NPs prefer the surface OR mechanism. At 500 K, the $t_{1/2}$ for supported Ag as an intermediate is 3 orders of magnitudes lower than that for

https://doi.org/10.1021/acs.jpcc.2c00612
J. Phys. Chem. C 2022, 126, 8056−8064

supported AgO. This difference in $t_{1/2}$ will further decrease as T decreases, and $t_{1/2}$ of supported AgO will be smaller than that of supported Ag below 300 K. This change in the ripening intermediate is consistent with the experimental observation that at 300 K, O_2 can accelerate the growth of Ag NPs at the cost of smaller ones on TiO_2(110) at 10 torr O_2.[59] Similar to Ag, the supported Pd atoms are also the dominant Pd ripening intermediates under an O_2 condition (Figure 6d), and the dominant ripening intermediate will also switch from Pd to PdO in the higher p of O_2 and lower T. However, it has about 4 orders of magnitude higher $t_{1/2}$ compared to Ag, therefore the OR for Pd NPs is relatively slower.

The difference between Pt, Pd, and Ag in ripening mechanisms is mainly due to the binding of ripening intermediates with support, as shown in Figure 3. For Pd and Ag, surface OR usually dominates since the supported monomers have a binding with the support compared to their gaseous compartments as strong as −2.53 eV (PdO) and −2.14 eV (AgO), therefore a higher intermediate density. However, when the corresponding gaseous compartments show additional stabilities, leading to the binding energy of PtO_2 with the TiO_2 surface as small as −0.34 eV, the gaseous OR becomes dominant. These models can be used as a basic tool for distinguishing these dominant sintering mechanisms, and the corresponding results inspire the strategy of suppressing dominant ripening mechanisms: for surface OR, we can modify the support to increase the diffusion barrier of surface monomers;[26,60] for gaseous OR, we can protect the volatile sites of the metals with other stable substances to prevent the formation of gaseous metal−oxygen complexes.[61]

To provide more chemical insights, we performed crystal orbital Hamilton population (COHP) for a TiO_2(110)-supported Ag atom and NiO and PtO_2 molecules, as shown in Figure S6, where integrated COHP (ICOHP) up to the Fermi level was also calculated to determine the strength of the chemical bond of interests. For the supported Ag atom (Figure S6a), it can be found that both bonding states and antibonding states are largely occupied. As a result, the chemical bond formed with respect to the substrate underneath is relatively weak, and the corresponding ICOHP of −0.80 eV is small. Whereas, for supported NiO molecules, the considerable antibonding states of Ni to oxygen of NiO (Figure S6b) and lattice oxygen (Figure S6c) are unoccupied, and the chemical bonds formed with a more negative ICOHP of −2.76 and −3.39 eV become stronger. Accordingly, the interaction of the NiO molecule to the support is strengthened. For the PtO_2 molecule (Figure S6d), the antibonding states between Pt and O of PtO_2 are nearly fully unoccupied, indicating a strong chemical bond formed along with the most negative ICOHP of −7.12 eV. As a result, the PtO_2 molecule interacts weakly with the support, in line with the energetics calculation. We performed a Bader charge analysis for supported Ni, Cu, Pd, Ag, and Pt atoms and the corresponding molecules on TiO_2(110), as shown in Table S2. It can be found that for the supported metal atoms, there are pronounced charge transfers from Ni, Cu, and Ag to the support. The charge transfer becomes modest for Pd and Pt due to the nature of the noble metals. Whereas, for supported oxide molecules, there is pronounced enhancement in charge transfer by more than 0.5 electron for Pd and Pt for their flexibility to a higher oxidation state. In Figure S7, we plot the charge difference for the supported NiO molecule. The charge depletion for Ni and accumulation for O of NiO and bridge oxygen can be clearly seen.

4. CONCLUSIONS

We used thermodynamics and kinetics simulation methods to study the disintegration and OR of Ni, Cu, Pt, Pd, and Ag NPs under O_2 conditions. The result shows that these metals have significantly different behaviors under an O_2 atmosphere. These differences can be rationalized by the interaction between metal atoms or metal−oxygen complexes and support. Oxygen induces the oxidation of Cu and the disintegration of Ni into a NiO complex due to the strong binding of the NiO complex with support. Pt can form volatile gaseous PtO_2 and it has a weak interaction with support, leading to its gaseous OR mechanism. Compared to the other metals, Ag and Pd have a moderate interaction with support but also the weakest interaction with oxygen, and surface OR occurs through surface Ag/Ag−O complexes or Pd atoms. These results provide valuable suggestions for the rational design of the supported metal NPs to maintain their designed structures under reaction conditions.

■ ASSOCIATED CONTENT

Supporting Information

The Supporting Information is available free of charge at https://pubs.acs.org/doi/10.1021/acs.jpcc.2c00612.

Additional figures and tables illustrating benchmarks of the energies, species with multiple metal atoms, and energy comparison of oxidation and disintegration (PDF)

■ AUTHOR INFORMATION

Corresponding Authors

Sulei Hu − *Department of Chemical Physics, School of Chemistry and Materials Science, Hefei National Research Center for Physical Sciences at the Microscale, University of Science and Technology of China, Hefei 230026 Anhui, China*; Email: husulei@ustc.edu.cn

Wei-Xue Li − *Department of Chemical Physics, School of Chemistry and Materials Science, Hefei National Research Center for Physical Sciences at the Microscale, University of Science and Technology of China, Hefei 230026 Anhui, China*; orcid.org/0000-0002-5043-3088; Email: wxli70@ustc.edu.cn

Authors

Shiyan Cao − *Department of Chemical Physics, School of Chemistry and Materials Science, Hefei National Research Center for Physical Sciences at the Microscale, University of Science and Technology of China, Hefei 230026 Anhui, China*

Xuting Chai − *Department of Chemical Physics, School of Chemistry and Materials Science, Hefei National Research Center for Physical Sciences at the Microscale, University of Science and Technology of China, Hefei 230026 Anhui, China*

Complete contact information is available at: https://pubs.acs.org/10.1021/acs.jpcc.2c00612

Notes

The authors declare no competing financial interest.

https://doi.org/10.1021/acs.jpcc.2c00612
J. Phys. Chem. C 2022, 126, 8056−8064

■ ACKNOWLEDGMENTS

This work was supported by the National Key R&D Program of China (2018YFA0208603 and 2021YFB3502000), the National Natural Science Foundation of China (91945302 and 21903077), the Chinese Academy of Sciences (QYZDJ-SSW-SLH054), the K. C. Wong Education (GJTD-2020-15), the Dalian National Laboratory For Clean Energy (DNL) Cooperation Fund, the CAS (DNL201920), the China Postdoctoral Science Foundation, the Fundamental Research Funds for the Central Universities, and the USTC Research Funds of the Double First-Class Initiative (KY9990000170). The authors thank the Supercomputing Center of the University of Science and Technology of China.

■ REFERENCES

(1) Ye, R. P.; Ding, J.; Gong, W.; Argyle, M. D.; Zhong, Q.; Wang, Y.; Russell, C. K.; Xu, Z.; Russell, A. G.; Li, Q.; et al. CO_2 Hydrogenation to High-Value Products via Heterogeneous Catalysis. *Nat. Commun.* **2019**, *10*, No. 5698.

(2) Bae, K. L.; Kim, J.; Lim, C. K.; Nam, K. M.; Song, H. Colloidal Zinc Oxide-Copper(I) Oxide Nanocatalysts for Selective Aqueous Photocatalytic Carbon Dioxide Conversion into Methane. *Nat. Commun.* **2017**, *8*, No. 1156.

(3) Beniya, A.; Higashi, S. Towards Dense Single-Atom Catalysts for Future Automotive Applications. *Nat. Catal.* **2019**, *2*, 590−602.

(4) Zhou, Y.; Jin, C.; Li, Y.; Shen, W. Dynamic Behavior of Metal Nanoparticles for Catalysis. *Nano Today* **2018**, *20*, 101−120.

(5) Kawaguchi, T.; Keller, T. F.; Runge, H.; Gelisio, L.; Seitz, C.; Kim, Y. Y.; Maxey, E. R.; Cha, W.; Ulvestad, A.; Hruszkewycz, S. O.; et al. Gas-Induced Segregation in Pt-Rh Alloy Nanoparticles Observed by in Situ Bragg Coherent Diffraction Imaging. *Phys. Rev. Lett.* **2019**, *123*, No. 246001.

(6) Kwon, O.; Sengodan, S.; Kim, K.; Kim, G.; Jeong, H. Y.; Shin, J.; Ju, Y. W.; Han, J. W.; Kim, G. Exsolution Trends and Co-Segregation Aspects of Self-Grown Catalyst Nanoparticles in Perovskites. *Nat. Commun.* **2017**, *8*, No. 15967.

(7) Yuan, W.; Zhang, D.; Ou, Y.; Fang, K.; Zhu, B.; Yang, H.; Hansen, T. W.; Wagner, J. B.; Zhang, Z.; Gao, Y.; Wang, Y. Direct in Situ Tem Visualization and Insight into the Facet-Dependent Sintering Behaviors of Gold on TiO_2. *Angew. Chem., Int. Ed.* **2018**, *57*, 16827−16831.

(8) Parkinson, G. S.; Novotny, Z.; Argentero, G.; Schmid, M.; Pavelec, J.; Kosak, R.; Blaha, P.; Diebold, U. Carbon Monoxide-Induced Adatom Sintering in a Pd-Fe_3O_4 Model Catalyst. *Nat. Mater.* **2013**, *12*, 724−728.

(9) Luo, L.; Engelhard, M. H.; Shao, Y.; Wang, C. Revealing the Dynamics of Platinum Nanoparticle Catalysts on Carbon in Oxygen and Water Using Environmental TEM. *ACS Catal.* **2017**, *7*, 7658−7664.

(10) Hulva, J.; Meier, M.; Bliem, R.; Jakub, Z.; Kraushofer, F.; Schmid, M.; Diebold, U.; Franchini, C.; Parkinson, G. S. Unraveling CO Adsorption on Model Single-Atom Catalysts. *Science* **2021**, *371*, 375−379.

(11) Bliem, R.; van der Hoeven, J. E.; Hulva, J.; Pavelec, J.; Gamba, O.; de Jongh, P. E.; Schmid, M.; Blaha, P.; Diebold, U.; Parkinson, G. S. Dual Role of CO in the Stability of Subnano Pt Clusters at the Fe_3O_4(001) Surface. *Proc. Natl. Acad. Sci. U.S.A.* **2016**, *113*, 8921−8926.

(12) Wang, F.; Ma, J.; Xin, S.; Wang, Q.; Xu, J.; Zhang, C.; He, H.; Cheng Zeng, X. Resolving the Puzzle of Single-Atom Silver Dispersion on Nanosized Gamma-Al_2O_3 Surface for High Catalytic Performance. *Nat. Commun.* **2020**, *11*, No. 529.

(13) Wei, S.; Li, A.; Liu, J. C.; Li, Z.; Chen, W.; Gong, Y.; Zhang, Q.; Cheong, W. C.; Wang, Y.; Zheng, L.; et al. Direct Observation of Noble Metal Nanoparticles Transforming to Thermally Stable Single Atoms. *Nat. Nanotechnol.* **2018**, *13*, 856−861.

(14) Zhu, B.; Meng, J.; Yuan, W.; Zhang, X.; Yang, H.; Wang, Y.; Gao, Y. Reshaping of Metal Nanoparticles under Reaction Conditions. *Angew. Chem., Int. Ed.* **2020**, *59*, 2171−2180.

(15) He, Y.; Liu, J. C.; Luo, L.; Wang, Y. G.; Zhu, J.; Du, Y.; Li, J.; Mao, S. X.; Wang, C. Size-Dependent Dynamic Structures of Supported Gold Nanoparticles in CO Oxidation Reaction Condition. *Proc. Natl. Acad. Sci. U.S.A.* **2018**, *115*, 7700−7705.

(16) Vendelbo, S. B.; Elkjaer, C. F.; Falsig, H.; Puspitasari, I.; Dona, P.; Mele, L.; Morana, B.; Nelissen, B. J.; van Rijn, R.; Creemer, J. F.; et al. Visualization of Oscillatory Behaviour of Pt Nanoparticles Catalysing CO Oxidation. *Nat. Mater.* **2014**, *13*, 884−890.

(17) Chang, Q.; Zhang, C.; Liu, C.; Wei, Y.; Cheruvathur, A. V.; Dugulan, A. I.; Niemantsverdriet, J. W.; Liu, X.; He, Y.; Qing, M.; et al. Relationship between Iron Carbide Phases (E-Fe_2C, Fe_7C_3, and X-Fe_5C_2) and Catalytic Performances of Fe/SiO_2 Fischer−Tropsch Catalysts. *ACS Catal.* **2018**, *8*, 3304−3316.

(18) Preikschas, P.; Plodinec, M.; Bauer, J.; Kraehnert, R.; Naumann d'Alnoncourt, R.; Schlögl, R.; Driess, M.; Rosowski, F. Tuning the Rh−Feox Interface in Ethanol Synthesis through Formation Phase Studies at High Pressures of Synthesis Gas. *ACS Catal.* **2021**, *11*, 4047−4060.

(19) Goodman, E. D.; Johnston-Peck, A. C.; Dietze, E. M.; Wrasman, C. J.; Hoffman, A. S.; Abild-Pedersen, F.; Bare, S. R.; Plessow, P. N.; Cargnello, M. Catalyst Deactivation by Decomposition into Single Atoms is Suppressed by Increasing Metal Loading. *Nat. Catal.* **2019**, *2*, 748−755.

(20) LaGrow, A. P.; Ward, M. R.; Lloyd, D. C.; Gai, P. L.; Boyes, E. D. Visualizing the Cu/Cu_2(O) Interface Transition in Nanoparticles with Environmental Scanning Transmission Electron Microscopy. *J. Am. Chem. Soc.* **2017**, *139*, 179−185.

(21) van Spronsen, M. A.; Frenken, J. W. M.; Groot, I. M. N. Observing the Oxidation of Platinum. *Nat. Commun.* **2017**, *8*, No. 429.

(22) Xia, G.; Tan, Y.; Chen, X.; Sun, D.; Guo, Z.; Liu, H.; Ouyang, L.; Zhu, M.; Yu, X. Monodisperse Magnesium Hydride Nanoparticles Uniformly Self-Assembled on Graphene. *Adv. Mater.* **2015**, *27*, 5981−5988.

(23) O'Brien, C. P.; Jenness, G. R.; Dong, H.; Vlachos, D. G.; Lee, I. C. Deactivation of Pt/Al_2O_3 During Propane Oxidation at Low Temperatures: Kinetic Regimes and Platinum Oxide Formation. *J. Catal.* **2016**, *337*, 122−132.

(24) DeRita, L.; Resasco, J.; Dai, S.; Boubnov, A.; Thang, H. V.; Hoffman, A. S.; Ro, I.; Graham, G. W.; Bare, S. R.; Pacchioni, G.; et al. Structural Evolution of Atomically Dispersed Pt Catalysts Dictates Reactivity. *Nat. Mater.* **2019**, *18*, 746−751.

(25) Zhang, H. B.; Liu, G. G.; Shi, L.; Ye, J. H. Single-Atom Catalysts: Emerging Multifunctional Materials in Heterogeneous Catalysis. *Adv. Energy Mater.* **2018**, *8*, No. 1701343.

(26) Li, G. X.; Fang, K.; Chen, Y. Z.; Ou, Y.; Mao, S. J.; Yuan, W. T.; Wang, Y.; Yang, H. S.; Zhang, Z.; Wang, Y. Unveiling the Gas-Dependent Sintering Behavior of Au-TiO_2 Catalysts Via Environmental Transmission Electron Microscopy. *J. Catal.* **2020**, *388*, 84−90.

(27) Li, R.; Xu, X.; Zhu, B.; Li, X. Y.; Ning, Y.; Mu, R.; Du, P.; Li, M.; Wang, H.; Liang, J.; et al. In Situ Identification of the Metallic State of Ag Nanoclusters in Oxidative Dispersion. *Nat. Commun.* **2021**, *12*, No. 1406.

(28) Moliner, M.; Gabay, J. E.; Kliewer, C. E.; Carr, R. T.; Guzman, J.; Casty, G. L.; Serna, P.; Corma, A. Reversible Transformation of Pt Nanoparticles into Single Atoms inside High-Silica Chabazite Zeolite. *J. Am. Chem. Soc.* **2016**, *138*, 15743−15750.

(29) Parker, S. C.; Campbell, C. T. Kinetic Model for Sintering of Supported Metal Particles with Improved Size-Dependent Energetics and Applications to Au on TiO_2(110). *Phys. Rev. B* **2007**, *75*, No. 035430.

(30) Wynblatt, P.; Gjostein, N. A. Model Study of Catalyst Particle Coarsening. *Scr. Mater.* **1973**, *7*, 969−975.

https://doi.org/10.1021/acs.jpcc.2c00612
J. Phys. Chem. C 2022, 126, 8056−8064

(31) Ouyang, R.; Liu, J. X.; Li, W. X. Atomistic Theory of Ostwald Ripening and Disintegration of Supported Metal Particles under Reaction Conditions. *J. Am. Chem. Soc.* **2013**, *135*, 1760−1771.
(32) Plessow, P. N.; Abild-Pedersen, F. Sintering of Pt Nanoparticles Via Volatile Pto2: Simulation and Comparison with Experiments. *ACS Catal.* **2016**, *6*, 7098−7108.
(33) Tran, R.; Xu, Z.; Radhakrishnan, B.; Winston, D.; Sun, W.; Persson, K. A.; Ong, S. P. Surface Energies of Elemental Crystals. *Sci. Data* **2016**, *3*, No. 160080.
(34) Kresse, G.; Hafner, J. Ab Initio Molecular Dynamics for Liquid Metals. *Phys. Rev. B* **1993**, *47*, 558−561.
(35) Kresse, G.; Furthmüller, J. Efficiency of Ab-Initio Total Energy Calculations for Metals and Semiconductors Using a Plane-Wave Basis Set. *Comput. Mater. Sci.* **1996**, *6*, 15−50.
(36) Kresse, G.; Furthmuller, J. Efficient Iterative Schemes for Ab Initio Total-Energy Calculations Using a Plane-Wave Basis Set. *Phys. Rev. B* **1996**, *54*, 11169−11186.
(37) Kresse, G.; Joubert, D. From Ultrasoft Pseudopotentials to the Projector Augmented-Wave Method. *Phys. Rev. B* **1999**, *59*, 1758−1775.
(38) Perdew, J. P.; Burke, K.; Ernzerhof, M. Generalized Gradient Approximation Made Simple. *Phys. Rev. Lett.* **1996**, *77*, 3865−3868.
(39) Burdett, J. K.; Hughbanks, T.; Miller, G. J.; Richardson, J. W.; Smith, J. V. Structural-Electronic Relationships in Inorganic Solids: Powder Neutron Diffraction Studies of the Rutile and Anatase Polymorphs of Titanium Dioxide at 15 and 295 K. *J. Am. Chem. Soc.* **1987**, *109*, 3639−3646.
(40) Kittel, C. *Introduction to Solid State Physics*, 8th ed.; John Wiley & Sons: Hoboken, NJ, 2005.
(41) Henkelman, G.; Uberuaga, B. P.; Jonsson, H. A Climbing Image Nudged Elastic Band Method for Finding Saddle Points and Minimum Energy Paths. *J. Chem. Phys.* **2000**, *113*, 9901−9904.
(42) Henkelman, G.; Jonsson, H. A Dimer Method for Finding Saddle Points on High Dimensional Potential Surfaces Using only First Derivatives. *J. Chem. Phys.* **1999**, *111*, 7010−7022.
(43) Larsen, A. H.; Mortensen, J. J.; Blomqvist, J.; Castelli, I. E.; Christensen, R.; Dulak, M.; Friis, J.; Groves, M. N.; Hammer, B.; Hargus, C.; et al. The Atomic Simulation Environment-a Python Library for Working with Atoms. *J. Phys.: Condens. Matter* **2017**, *29*, No. 273002.
(44) Reuter, K.; Scheffler, M. Composition and Structure of the RuO_2 (110) Surface in an O_2 and CO Environment: Implications for the Catalytic Formation of CO_2. *Phys. Rev. B* **2003**, *68*, No. 045407.
(45) Berglund, S. The Free Energy of Formation of Nickel Oxide. *Ber. Bunsenges. Phys. Chem.* **1976**, *80*, 862−866.
(46) Holmes, R. D.; Kersting, A. B.; Arculus, R. J. Standard Molar Gibbs Free Energy of Formation for Cu_2O: High-Resolution Electrochemical Measurements from 900 to 1300 K. *J. Chem. Thermodyn.* **1989**, *21*, 351−361.
(47) Ono, L. K.; Yuan, B.; Heinrich, H.; Cuenya, B. R. Formation and Thermal Stability of Platinum Oxides on Size-Selected Platinum Nanoparticles: Support Effects. *J. Phys. Chem. C* **2010**, *114*, 22119−22133.
(48) Warner, J. S. The Free Energy of Formation of Palladium Oxide. *J. Electrochem. Soc.* **1967**, *114*, 68−71.
(49) Assal, J.; Hallstedt, B.; Gauckler, L. J. Thermodynamic Assessment of the Silver-Oxygen System. *J. Am. Ceram. Soc.* **2005**, *80*, 3054−3060.
(50) Zhou, J.; Kang, Y. C.; Ma, S.; Chen, D. A. Adsorbate-Induced Dissociation of Metal Clusters: TiO_2(110)-Supported Cu and Ni Clusters Exposed to Oxygen Gas. *Surf. Sci.* **2004**, *562*, 113−127.
(51) Zhou, J.; Kang, Y. C.; Chen, D. A. Oxygen-Induced Dissociation of Cu Islands Supported on TiO_2(110). *J. Phys. Chem. B* **2003**, *107*, 6664−6667.
(52) Zhou, J.; Kang, Y. C.; Ma, S.; Chen, D. A. Adsorbate-Induced Dissociation of Metal Clusters: TiO_2 (110)-Supported Cu and Ni Clusters Exposed to Oxygen Gas. *Surf. Sci.* **2004**, *562*, 113−127.
(53) Hu, S.; Li, W.-X. Influence of Particle Size Distribution on Lifetime and Thermal Stability of Ostwald Ripening of Supported Particles. *ChemCatChem* **2018**, *10*, 2900−2907.
(54) Hu, S.; Ouyang, R.; Li, W.-X. First-Principles Kinetics Study of Carbon Monoxide Promoted Ostwald Ripening of Au Particles on FeO/Pt(111). *J. Energy Chem.* **2019**, *30*, 108−113.
(55) Wan, Q.; Hu, S.; Dai, J.; Chen, C.; Li, W.-X. Influence of Crystal Facet and Phase of Titanium Dioxide on Ostwald Ripening of Supported Pt Nanoparticles from First-Principles Kinetics. *J. Phys. Chem. C* **2019**, *123*, 11020−11031.
(56) Arblaster, J. W. Thermodynamic Properties of Silver. *J. Phase Equilib. Diffus.* **2015**, *36*, 573−591.
(57) Arblaster, J. W. The Thermodynamic Properties of Platinum. *Platinum Met. Rev.* **2005**, *49*, 141−149.
(58) Tabib Zadeh Adibi, P.; Mazzotta, F.; Antosiewicz, T. J.; Skoglundh, M.; Grönbeck, H.; Langhammer, C. In Situ Plasmonic Sensing of Platinum Model Catalyst Sintering on Different Oxide Supports and in O_2 and NO_2 Atmospheres with Different Concentrations. *ACS Catal.* **2015**, *5*, 426−432.
(59) Lai, X.; St Clair, T. P.; Wayne Goodman, D. Oxygen-Induced Morphological Changes of Ag Nanoclusters Supported on TiO_2(110). *Faraday Discuss.* **1999**, *114*, 279−284.
(60) van den Berg, R.; Parmentier, T. E.; Elkjær, C. F.; Gommes, C. J.; Sehested, J.; Helveg, S.; de Jongh, P. E.; de Jong, K. P. Support Functionalization to Retard Ostwald Ripening in Copper Methanol Synthesis Catalysts. *ACS Catal.* **2015**, *5*, 4439−4448.
(61) Cai, J.; Zhang, J.; Cao, K.; Gong, M.; Lang, Y.; Liu, X.; Chu, S.; Shan, B.; Chen, R. Selective Passivation of Pt Nanoparticles with Enhanced Sintering Resistance and Activity toward CO Oxidation via Atomic Layer Deposition. *ACS Appl. Nano Mater.* **2018**, *1*, 522−530.

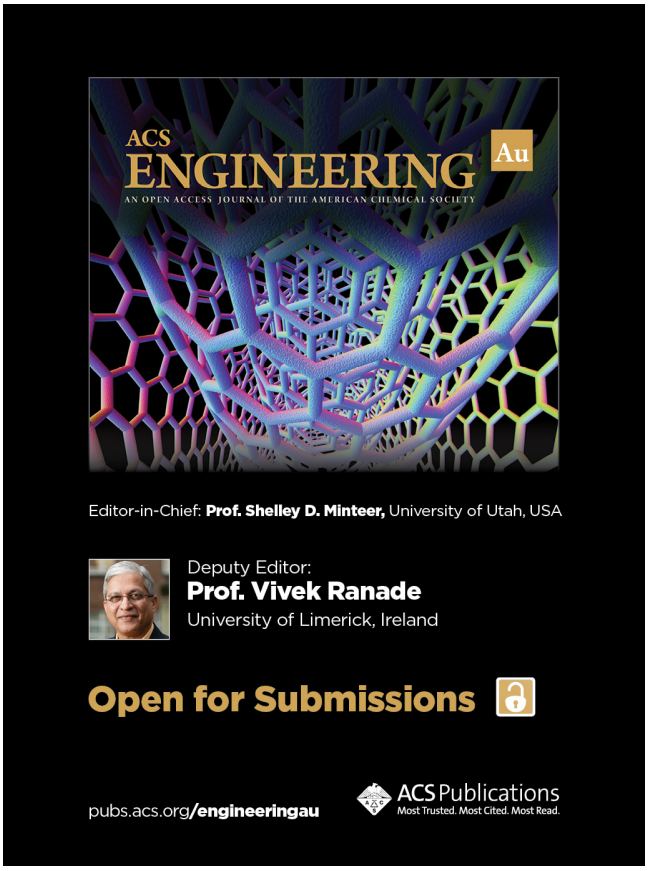

https://doi.org/10.1021/acs.jpcc.2c00612
J. Phys. Chem. C 2022, 126, 8056−8064